Volume 8
Number 10
October 2021
Pages 2587–2860

Materials Horizons

rsc.li/materials-horizons

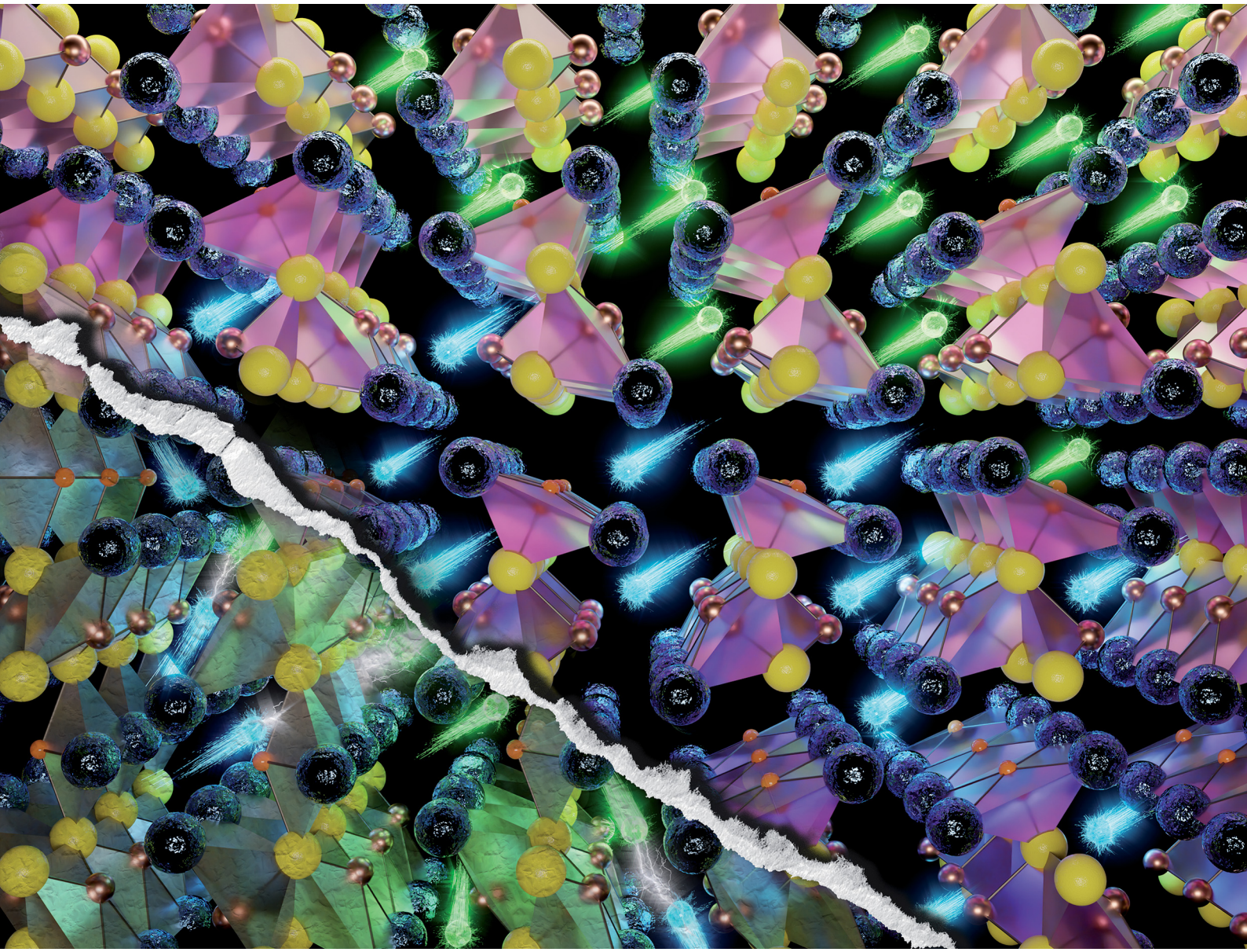

ISSN 2051-6347

ROYAL SOCIETY OF CHEMISTRY

COMMUNICATION

David O. Scanlon, Aron Walsh *et al.*

Hidden spontaneous polarisation in the chalcohalide photovoltaic absorber $Sn_2SbS_2I_3$

Materials Horizons

ROYAL SOCIETY OF CHEMISTRY

COMMUNICATION

View Article Online
View Journal | View Issue

Check for updates

Cite this: *Mater. Horiz.*, 2021, 8, 2709

Received 12th May 2021,
Accepted 1st July 2021

DOI: 10.1039/d1mh00764e

rsc.li/materials-horizons

Hidden spontaneous polarisation in the chalcohalide photovoltaic absorber $Sn_2SbS_2I_3$†

Seán R. Kavanagh, [ab] Christopher N. Savory, [a] David O. Scanlon *[ac] and Aron Walsh *[ad]

Perovskite-inspired materials aim to replicate the optoelectronic performance of lead-halide perovskites, while eliminating issues with stability and toxicity. Chalcohalides of group IV/V elements have attracted attention due to enhanced stability provided by stronger metal-chalcogen bonds, alongside compositional flexibility and ns^2 lone pair cations – a performance-defining feature of halide perovskites. Following the experimental report of solution-grown tin-antimony sulfoiodide ($Sn_2SbS_2I_3$) solar cells, with power conversion efficiencies above 4%, we assess the structural and electronic properties of this emerging photovoltaic material. We find that the reported centrosymmetric *Cmcm* crystal structure represents an average over multiple polar $Cmc2_1$ configurations. The instability is confirmed through a combination of lattice dynamics and molecular dynamics simulations. We predict a large spontaneous polarisation of 37 μC cm^{-2} that could be active for electron–hole separation in operating solar cells. We further assess the radiative efficiency limit of this material, calculating $\eta_{max} > 30\%$ for film thicknesses $t > 0.5$ μm.

New concepts

Mixed-metal chalcohalides have emerged at the forefront of perovskite-inspired materials. A rigorous description of their atomistic properties and performance potential is lacking. In particular, $Sn_2SbS_2I_3$ contains two lone-pair cations which are known to drive unusual structure–property relations. Using a range of first-principles modelling techniques, we reveal a spontaneous symmetry breaking away from the known non-polar crystal structure. We link this local polarisation, which was previously hidden to macroscopic diffraction techniques, to the high optoelectronic efficiency potential and defect-tolerant properties of this system. The results shine a spotlight on the largely-unexplored class of $A_2BCh_2X_3$ mixed-metal chalcohalides. These are candidates for solution-processed ferroelectric and optoelectronic devices, with the substitutional flexibility for engineering band gaps, band energies, and lattice polarisation.

The photovoltaic performance of lead-halide perovskites has spurred major research efforts toward the discovery of 'perovskite-inspired materials' (PIMs).[1–3] Through the use of lead-free and stable alternative materials, PIMs aim to replicate the ability of halide perovskites to combine high optoelectronic performance with low-cost solution processing methods, while overcoming their infamous stability and toxicity drawbacks. The applications of PIMs are not solely limited to solar cell devices. In fact, these materials have seen successful implementation in a wide range of optoelectronic applications, such as light-emitting diodes, photocatalysts, radiation detectors, thin film transistors and memristors.[1]

A defining feature of halide perovskites is the combination of a lone-pair cation with a halide anion which can produce, *inter alia*, dispersive valence and conduction bands, defect tolerance, and strong dielectric screening.[1,4] On the other hand, the soft metal-halide bonding contributes to the poor chemical and thermal stabilities of these materials.[5] Chalcohalide PIMs offer a route around this issue, demonstrating remarkably higher air and water stability – due to the increased strength of metal-chalcogen bonding[4,5] – while retaining the ns^2 cation–halide anion combination. These materials have already demonstrated promising efficiencies (>4%[1,6,7]) alongside low-cost fabrication methods, representing a fertile area for stable, non-toxic high-performance solar cells.[8] Further increases in power-conversion efficiencies (PCEs) will be required to achieve commercial viability.[5]

Here we focus on tin antimony sulfoiodide ($Sn_2SbS_2I_3$). Olivier-Fourcade *et al.*[9] reported the preparation and structural characterisation of $Sn_2SbS_2I_3$ in 1980, determining an orthorhombic *Cmcm* space group using X-ray diffraction measurements. This work was followed up with single-crystal X-ray analysis by the same

[a] *Department of Chemistry & Thomas Young Centre, University College London, 20 Gordon Street, London WC1H 0AJ, UK. E-mail: d.scanlon@ucl.ac.uk, a.walsh@imperial.ac.uk*
[b] *Department of Materials & Thomas Young Centre, Imperial College London, Exhibition Road, London SW7 2AZ, UK*
[c] *Diamond Light Source Ltd., Diamond House, Harwell Science and Innovation Campus, Didcot, Oxfordshire OX11 0DE, UK*
[d] *Department of Materials Science and Engineering, Yonsei University, Seoul 03722, Republic of Korea*

† Electronic supplementary information (ESI) available: Additional structural, dielectric, electronic and optical analysis. See DOI: 10.1039/d1mh00764e

Open Access Article. Published on 05 July 2021. Downloaded on 6/18/2025 2:58:34 AM.
This article is licensed under a Creative Commons Attribution 3.0 Unported Licence.

Open Access Article. Published on 05 July 2021. Downloaded on 6/18/2025 2:58:34 AM.
This article is licensed under a Creative Commons Attribution 3.0 Unported Licence.

research group in 1984.[10] Later, Dolgikh[11] prepared both $Sn_2SbS_2I_3$ and the isostructural, isoelectronic $Pb_2SbS_2I_3$ compound and investigated the optical dielectric response. Then in 1990, Starosta *et al.*[12] prepared both antimony sulfoiodide compounds and used photoconductivity measurements to determine optical band gaps of 1.5 and 2.0 eV for the Sn and Pb-based materials, respectively. They also discussed the seemingly anomalous trend of increased band gap with chemical substitution of heavier elements.

In a major breakthrough, $Sn_2SbS_2I_3$ was recently reported to exhibit a photovoltaic efficiency exceeding 4% in the first experimental device fabrication.[4] Nie *et al.* used a low-cost single-step deposition method and reported good stability under conditions of high temperature, humidity and illumination. The achievement of a power conversion efficiency exceeding that first reported for methylammonium lead-iodide (MAPI)[13] is promising. While $Sn_2SbS_2I_3$ has been known for several decades,[9] it is now at the forefront of potential defect-tolerant PIMs for optoelectronic applications. In this work, we characterise the physical properties of $Sn_2SbS_2I_3$ using *ab initio* methods in order to understand the atomistic origins of impressive PV performance, and to assess the efficiency potential going forward.

Computational methods

We employ a combination of methods to probe the static and dynamic crystal structure of $Sn_2SbS_2I_3$, in addition to its electronic and optical properties. All base calculations were performed using Density Functional Theory (DFT) within periodic boundary conditions through the Vienna *Ab Initio* Simulation Package (VASP).[14–17] After testing several DFT exchange–correlation functionals (Section S2.2, ESI†), the optB86b-vdW[18] functional was chosen for geometry optimisation, yielding the closest agreement with experiment for the *c*/*a* lattice parameter ratio. The ability of this dispersion-corrected functional to incorporate van der Waals interactions in solids has been well demonstrated, yielding accurate predictions of lattice parameters in lone-pair materials.[19–22] To calculate relative formation energies and the ferroelectric-switching barrier with accuracy beyond DFT, the Random Phase Approximation (RPA) to the correlation energy was employed, using electronic wavefunctions calculated with the HSE06[23] screened hybrid DFT functional.[24,25] The HSE06 functional, with full inclusion of spin–orbit coupling effects, was also used for calculations of optical and electronic behaviour – having been demonstrated to yield accurate predictions of band gaps in semiconductor materials.[26,27] Comprehensive details of the computational implementation are provided in Section S1 of the ESI,† and all calculation data and analyses are provided in an online repository at doi.org/10.5281/zenodo.4683140.

Structural analysis

Geometry optimisations were performed for $Sn_2SbS_2I_3$ in both *Cmcm* and *Cmc*2_1 space groups, using the entries on the Materials Project repository[28] as the starting points. The relaxed crystal structures and unit cell dimensions are provided in Fig. 1 and Table 1, respectively.

The *Cmcm* structure comprises infinite chains of $(Sn_2S_2I_2)_n$ along the *a* direction, tightly-packed along the *b* direction to form layers in the *ab* plane, with antimony and iodine atoms located between layers, yielding the overall $(Sn_2SbS_2I_3)_n$ stoichiometry. The $(Sn_2S_2I_2)_n$ chains are formed from face-sharing SnS_3I_2 pyramids, comprising a parallelepid base of S_2I_2 and an apical sulfur atom. In fact, this $(Sn_2S_2I_2)_n$ structural motif matches the 1D chain structures of the AChX (A = Bi, Sb; Ch = S, Se; X = Br, I) ns^2-cation chalcohalide family.[29–32] Moving to the *Cmc*2_1 crystal structure, the coordination environments of Sb and (to a lesser extent) Sn shift to produce connected chains of the formula unit $(Sn_2SbS_2I_3)_n$ along the *a* direction, as the Sb atoms attach to the $(Sn_2S_2I_2)_n$ layers. The *a* and *b* cell lengths are similar for both polymorphs, with the greatest difference occurring along the *c* direction.

Much of the structural behaviour in this system is governed by the lone-pair activities of Sb(III) and Sn(II) cations. While the antimony cations are found to exhibit significant localisation of the ns^2 electrons, only minimal distortion from spherical symmetry is witnessed for the Sn(II) lone-pair, due to a preferential alignment and thus enhanced interaction with anion p states (Section S3, ESI†). In both polymorphs, the Sb lone-pair is directed toward halide-bordered voids; either *along* the inter-chain gap (*b* direction) for *Cmcm* symmetry or *toward* the

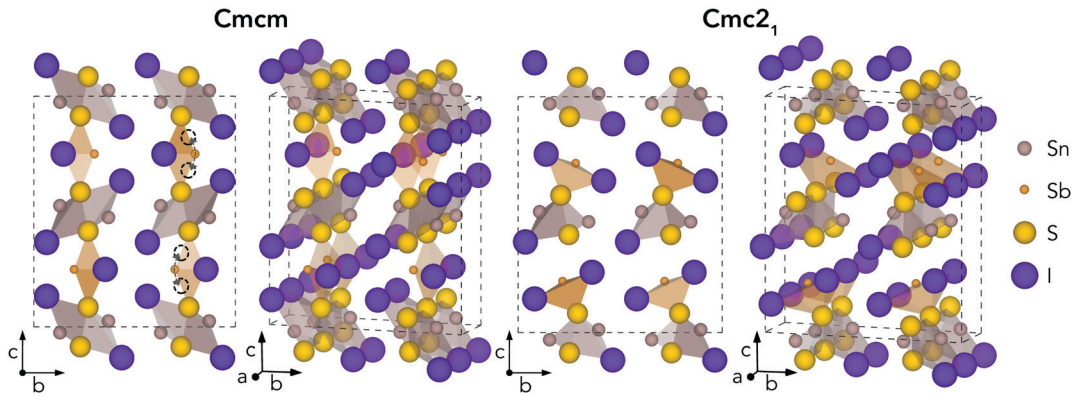

Fig. 1 Calculated crystal structures for *Cmcm* and *Cmc*2_1 polymorphs of $Sn_2SbS_2I_3$, in the conventional orthorhombic unit cell. Atoms sized according to their formal ionic radii. Curved arrows and empty circles indicate equivalent shifts in Sb position which correspond to the *Cmcm* to *Cmc*2_1 transition.

 This journal is © The Royal Society of Chemistry 2021

Open Access Article. Published on 05 July 2021. Downloaded on 6/18/2025 2:58:34 AM.
This article is licensed under a Creative Commons Attribution 3.0 Unported Licence.

Table 1 Calculated lattice parameters of the conventional orthorhombic unit cell for both polymorphs of $Sn_2SbS_2I_3$, using the optB86b-vdW DFT functional. Experimental values taken from low-temperature (T = 173 K) X-ray diffraction measurements[10]

	c/a	a/Å	b/Å	c/Å	Vol./Å^3
Cmcm	3.75	4.27	14.02	16.00	957.9
$Cmc2_1$	3.85	4.29	14.31	16.51	1013.8
Experiment	3.85	4.25	13.99	16.38	973.9

interchain gap (c direction) for $Cmc2_1$ – with more pronounced localisation visible in the $Cmc2_1$ case (Figs. S6–S8, ESI†). Indeed, this dynamic stereochemical activity of the Sb lone-pair is one of the primary driving factors behind the formation of the distorted, lower-symmetry $Cmc2_1$ polymorph – through a second-order Jahn–Teller instability, often observed in lone-pair chalcogenides.[22,33–35]

While all experimental works have reported the *Cmcm* crystal structure for $Sn_2SbS_2I_3$,[9,10,12] Ibanez *et al.*[10] noted that assignment of Sb to an 8f Wyckoff position (*i.e.* the Sb Wyckoff site in $Cmc2_1$ symmetry) with 50% occupancy, as opposed to the 4c site for *Cmcm*, gave a significant reduction in *R*-factor – a measure of agreement between the structure model and diffraction data[36] – from 0.105 to 0.066. Moreover, both Olivier-Fourcade *et al.*[9] and Ibanez *et al.*[10] observed large Debye–Waller (B) displacement factors for the Sb and Sn sites in $Sn_2SbS_2I_3$ (*i.e.* the site positions which differ most between *Cmcm* and $Cmc2_1$ structures), even at temperatures as low as T = 173 K, alongside large anisotropy in the atomic displacement ellipsoids. Further structural and lone-pair analysis, with direct comparison to experiment (Fig. S4, ESI†), is provided in Sections S2 and S3 (ESI†).

Thermodynamic & dynamic stability

To ensure a high level of accuracy in the calculated phase stabilities, the Random Phase Approximation (RPA) to the correlation energy was employed. This beyond-DFT method has been demonstrated to yield predictions in excellent agreement with experimental results for the relative formation energies of structural polymorphs.[1,38,39] With this method, the lower-symmetry $Cmc2_1$ phase was predicted to be the thermodynamically-favoured polymorph, with a formation energy 35.8 meV per atom below *Cmcm*.

Further evidence of *Cmcm* instability was obtained by computing the phonon dispersions of both $Sn_2SbS_2I_3$ polymorphs – shown in Fig. 2. Imaginary harmonic modes in the phonon dispersion (*i.e.* those with negative frequencies; $\omega < 0$) indicate the presence of atomic displacements which lower the system energy. Two strong imaginary modes are witnessed in the *Cmcm* dispersion, demonstrating dynamic structural instability for this polymorph. Using the ISODISTORT[40,41] package to visualise the imaginary-mode phonon eigenvectors, we confirm that these energy-lowering distortions correspond to different, equivalent *Cmcm* → $Cmc2_1$ structural transitions (Fig. S5, ESI†).

In contrast, no imaginary modes are observed for the $Cmc2_1$ polymorph. Thus we find the $Cmc2_1$ polymorph to exhibit both thermodynamic and dynamic stability, with converse behaviour for the *Cmcm* phase. We propose that experimental reports of *centrosymmetric Cmcm* $Sn_2SbS_2I_3$ are the result of macroscopic averaging over locally *non-centrosymmetric* $Cmc2_1$ configurations. Similar to other ns^2 cation materials,[22,29,33] this polar phase behaviour is driven by a second-order (pseudo) Jahn–Teller instability, in which the off-centring of the Sb(III) ions leads to enhanced bonding interactions between the sp-hybridised Sb ns^2 lone pair and the anion p states (yielding a small degree of Sb p character at 5 eV below the valence band maximum (VBM); Fig. 5a).

Spontaneous lattice polarisation

In the $Cmc2_1$ ground-state structure, the lack of inversion symmetry results in a spontaneous lattice polarisation ΔP = 37.0 μC cm^{-2} (calculated within the Berry phase formalism of the Modern Theory of Polarisation).[42] The strong polarity places $Sn_2SbS_2I_3$ next to the likes of ferroelectric oxide perovskites such as $BaTiO_3$ (~27 μC cm^{-2})[43] and $KNbO_3$ (~30 μC cm^{-2}), well above that of $MAPbI_3$ ('MAPI')(4.4 μC cm^{-2})[44] and the archetypal 'photoferroic' SbSI (11 μC cm^{-2}).[29,45] The mirror (m) and c-glide planes of the $Cmc2_1$ space group result in zero polarisation in

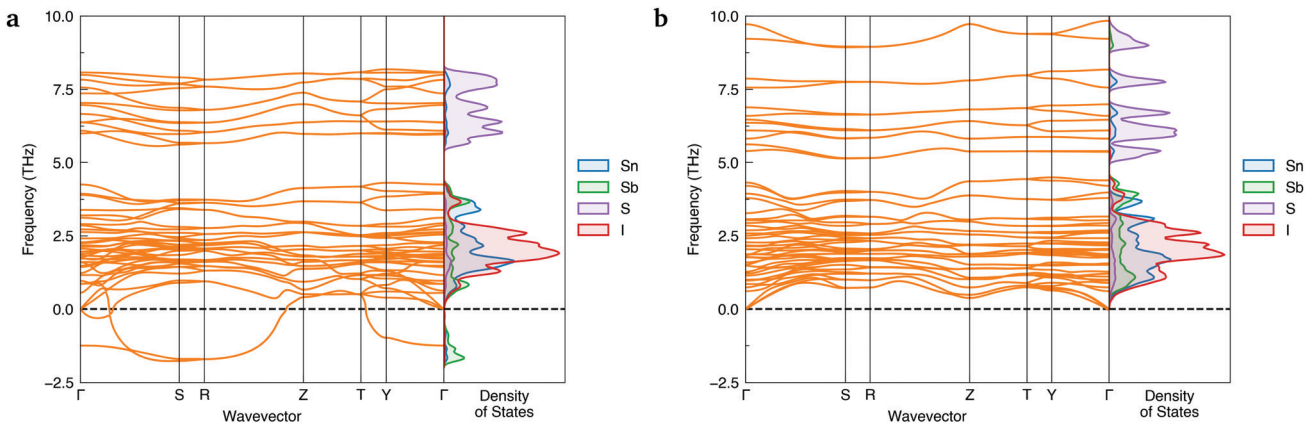

Fig. 2 Simulated harmonic phonon dispersions of $Sn_2SbS_2I_3$ in the *Cmcm* (a) and $Cmc2_1$ (b) crystal structures, alongside vertical plots of the atom-projected phonon density of states. Generated using ThermoPlotter.[37] Brillouin zone path shown in Section S10a (ESI†).

Open Access Article. Published on 05 July 2021. Downloaded on 6/18/2025 2:58:34 AM.
This article is licensed under a Creative Commons Attribution 3.0 Unported Licence.

the *ab* plane, with all electronic polarisation directed along the *c* axis, corresponding to the shift in Sb position indicated by the arrows in Fig. 1 and Fig. S5 (ESI†).

We identify substantial mixed ionic-covalent bonding character in this system, reminiscent of that found in ns^2-cation metal halides.[1,32,46] Significant covalency is indicated by the cross-band-gap hybridisation of both cation p orbitals with both anion p orbitals, demonstrated by their overlap in both the conduction and valence bands (Fig. 5 and Fig. S13, S22, ESI†). Further evidence of enhanced orbital overlap is derived from the reduced cation–anion distances, relative to their ionic radii, save for the Sb–I pair (Table S1, ESI†). The resulting mixed ionic-covalent bonding gives rise to strong lattice polarisation, with large, anisotropic Born effective charges (Table 2) and dielectric tensor ($\varepsilon_{x,y,z}$ = [51.3, 18.2, 22.4]).[1,32,47,48]

To calculate the barrier to polarisation switching, the Nudged Elastic Band (NEB)[50] method was employed to map out the potential energy surface (PES) along the minimum-energy path between equivalent $Cmc2_1$ configurations (Fig. 3).

We find that the *Cmcm* phase corresponds to the transition state between $Cmc2_1$ configurations, with no local stability around this saddle point on the PES. Consequently, the energetic barrier to ferroelectric switching corresponds to the relative energy of the *Cmcm* and $Cmc2_1$ polymorphs; ΔE = 35.8 meV per atom. This value gives rise to a moderate coercive field – calculated as 750 kV cm^{-1} for a single-crystal ferroelectric domain, using Landau theory (eqn (S1), ESI†).[51] While the actual value will likely be at least an order of magnitude below this, due to a number of effects including domain formation, it places this material in a range intermediate between the weakly-polar lead-halide perovskites[52] and the stronger oxide perovskites,[51] as might be expected for a lone-pair chalcohalide material.

To demonstrate the stability of lattice polarisation at finite temperatures, we performed Molecular Dynamics (MD) simulations for $Sn_2SbS_2I_3$ within an *NVT* ensemble at temperatures of 300 K and 500 K (Section S8, ESI†). Upon distortion from *Cmcm* to $Cmc2_1$, the two nearest-neighbour S atoms for Sb become inequivalent, forming short (in the polarisation direction) and long Sb–S bonds (Fig. 1 and Fig. S25, ESI†), allowing the polarisation dynamics to be visualised through the Sb–S bond lengths. As shown in Fig. 4, no appreciable swapping of the Sb–S bonds (corresponding to polarisation switching) is observed for the room-temperature MD runs, within the simulation timescale. On the other hand, transient hopping of Sb atoms occurs during the T = 500 K runs, as the material approaches a phase transition to higher-symmetry *Cmcm* (at which point the Sb–S bonds become equivalent and the probability densities merge; Fig. S25, ESI†), indicating a significant decrease in both the strength and stability of lattice polarisation at elevated temperatures. These results confirm the persistence of polar

Table 2 Mean Born effective charge tensors (Z^*_{ii}; |e|) for each atomic species in $Sn_2SbS_2I_3$, calculated using the optB86b-vdW DFT functional.[a] The Born effective charge is a measure of the relationship between polarisation and atomic displacement, and is greater for the *Cmcm* phase due to structural instability.[47,49] Comparison given to their formal oxidation states

Species	Ox. state	Z^*_{xx}	Z^*_{yy}	Z^*_{zz}
Sn, *Cmcm*	+2	+4.00	+3.00	+3.41
Sn, $Cmc2_1$	+2	+4.07	+3.16	+2.77
Sb, *Cmcm*	+3	+6.82	+3.55	+9.08
Sb, $Cmc2_1$	+3	+6.17	+2.84	+6.08
S, *Cmcm*	−2	−2.88	−2.44	−4.40
S, $Cmc2_1$	−2	−2.69	−2.47	−3.50
I, *Cmcm*	−1	−3.03	−1.55	−2.10
I, $Cmc2_1$	−1	−2.98	−1.41	−1.53

[a] Mean Born effective charges were calculated by taking the mean of the diagonal tensor component (Z^*_{ii}) for each atomic species. Full Z^*_{ij} tensors for each symmetry-inequivalent species are provided in Table S6 (ESI).

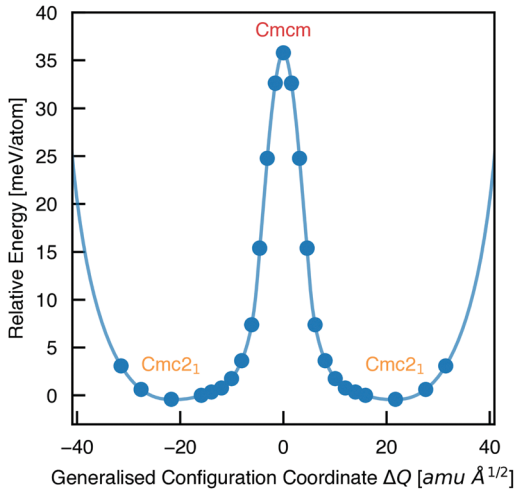

Fig. 3 Potential energy surface along the configurational path between equivalent $Cmc2_1$ configurations of $Sn_2SbS_2I_3$ (corresponding to the curved arrows in Fig. 1), calculated using the Nudged Elastic Band method.[50] Filled circles represent calculated data points and the solid line is a spline fit. *X* axis given in units of mass-weighted displacement.

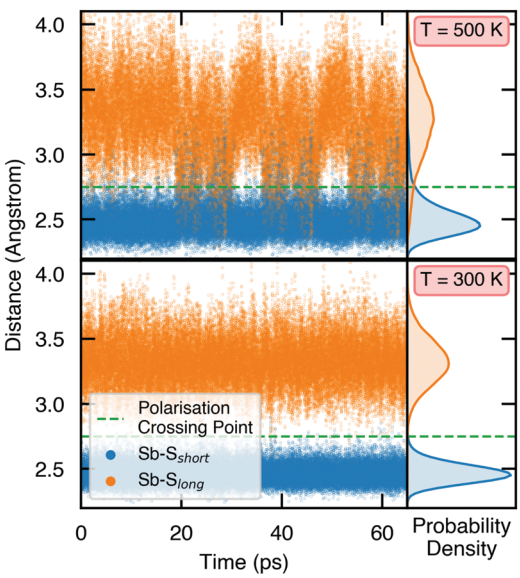

Fig. 4 Variation of Sb–S bond lengths in $Sn_2SbS_2I_3$ as a function of time during molecular dynamics simulations. The probability densities are shown on the right, given by $4\pi r^2 g(r)$, where $g(r)$ is the radial distribution function.

This journal is © The Royal Society of Chemistry 2021

Open Access Article. Published on 05 July 2021. Downloaded on 6/18/2025 2:58:34 AM.
This article is licensed under a Creative Commons Attribution 3.0 Unported Licence.

distortions at room temperature and dynamic fluctuations at 500 K. We cannot comment on the size of the polar domains that would be formed, however.

The presence of this previously-hidden polar distortion in $Sn_2SbS_2I_3$ poses several exciting prospects. In terms of PV applications, spontaneous polarisation can produce open-circuit voltages above the electronic band gap, *via* the Bulk Photovoltaic Effect, potentially allowing efficiencies above the standard limit for a single-junction solar cell.[53–56] Moreover, the combination of ferroelectric behaviour and spin–orbit coupling could permit switchable spin texture for 'ferroelectric Rashba semiconductor' applications,[57] while the effect on longitudinal optical (LO) phonons could favour polaron formation.[58]

Electronic structure

The electronic band structure of $Cmc2_1$ $Sn_2SbS_2I_3$ is shown in Fig. 4. The band gap is direct, occurring at the Y high-symmetry k-point – which corresponds to maximum antiphase interactions along the conventional *a* crystal direction (*i.e.* along the $(Sn_2SbS_2I_3)_n$ chains in Fig. 1). The fundamental energy gap is calculated as E_g = 1.08 eV, placing it in the ideal range for a photovoltaic absorber material, with a 'detailed-balance' efficiency limit of 32.5%.[62]

As illustrated by the orbital-projected density of states and band-edge charge densities in Fig. 5a and Fig. S13, S14 (ESI†), the conduction band minimum (CBM) arises from Sb p–I p interactions, while the VBM is comprised of antibonding interactions between the Sn $5s^2$ lone pair and both anion p states (Fig. 6). Notably, this electronic structure allows the explanation of the reported 'anomalous' trend in band gap energies within the $A_2SbS_2I_3$ (A = Sn, Pb) isostructure family, for which Starosta *et al.*[12] found a gap 0.5 eV *larger* for the Pb-based compound. While band gaps of conventional semiconductors tend to decrease upon substitution of heavier elements, due to increased orbital energies, we witness a strong contradiction to this trend in this material class. This behaviour occurs due to the relativistic contraction of the Pb 6s orbitals, so that the Sn 5s states are in fact higher in energy,[63] thus enhancing the anti-bonding interaction of the ns^2 lone-pair with the anion p states at the VBM (Fig. 6).[64] The result is a more disperse, higher-energy VBM with a reduced energy gap. See Section S6 (ESI†) for a discussion of the effects of spin–orbit interactions and the electronic structure of the *Cmcm* polymorph.

The optical absorption spectrum, shown in Fig. 4, exhibits a weak onset at the fundamental electronic band gap E_g = 1.08 eV. There are two primary origins of this behaviour. Firstly, we find a low electronic degeneracy at the band extrema (Fig. 5a and Fig. S16, S17, ESI†), itself a consequence of the low crystal symmetry, which rapidly increases with many more interband transitions available at $E \geq 1.4$ eV. Another contributing factor is a weak transition dipole moment between the VBM and CBM electronic states (Fig. S15–S17, ESI†) – a consequence of both symmetry restriction and low spatial overlap. In the centrosymmetric *Cmcm* structure, the even (*gerade*) parity of both the VBM and CBM wavefunctions about the crystal inversion centre results in a formally symmetry-forbidden transition at the direct gap (as the electric dipole operator is of odd parity, thus yielding an overall zero optical transition matrix element; Section S6, ESI†). For the $Cmc2_1$ ground-state polymorph, this symmetry selection rule is broken by the shift in Sb positions (removing the inversion symmetry) as well as spin–orbit splitting, however these effects represent a relatively minor perturbation to the electronic structure ($\Delta E_{g,Cmcm\,vs.\,Cmc21}$ = 0.03 eV; Fig. S11, ESI†). Consequently, while the direct VBM → CBM transition is no longer formally forbidden in the $Cmc2_1$ structure, the optical transition matrix element remains weak due to symmetry restraints, compounded by a spatial separation of the VBM and CBM states (Fig. S14, ESI†). The combination of a rapidly increasing joint density of states

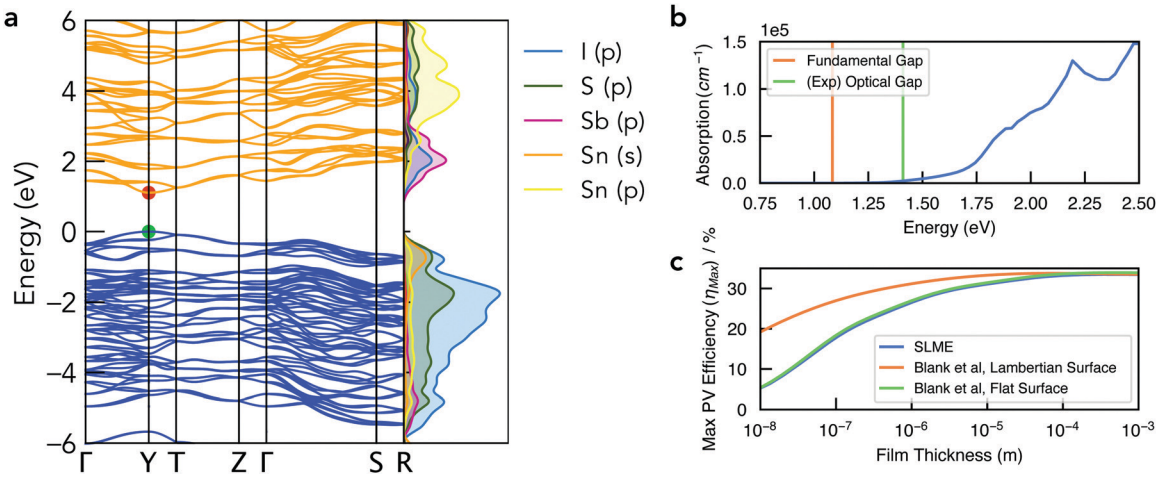

Fig. 5 (a) Electronic band structure of $Sn_2SbS_2I_3$ in the $Cmc2_1$ crystal structure, alongside a vertical plot of the orbital-projected electronic density of states, generated using sumo.[59] Valence band in blue, conduction band in orange, and VBM set to 0 eV. Brillouin zone path shown in Fig. S10b (ESI†). (b) Absorption spectrum with vertical lines indicating the calculated electronic band gap and the experimental optical gap (Ref: Nie *et al.*[4]). Note that spectral smearing is expected under experimental measurement. (c) Maximum PV efficiency (η_{max}) as a function of film thickness, using the SLME[60] and Blank *et al.*[61] estimates for the radiative limit (Q_i = 1).

Open Access Article. Published on 05 July 2021. Downloaded on 6/18/2025 2:58:34 AM.
This article is licensed under a Creative Commons Attribution 3.0 Unported Licence.

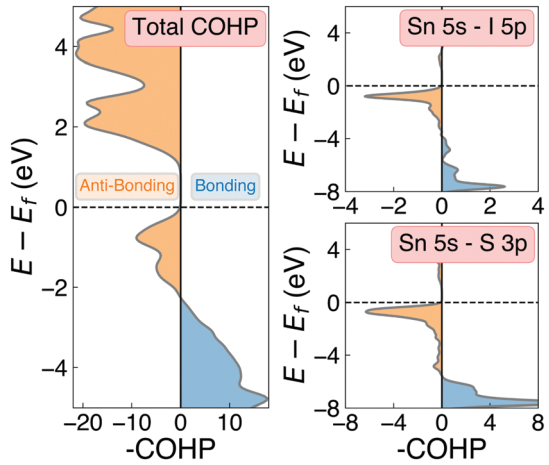

Fig. 6 COHP(E) cumulative (left) and Sn 5s – anion p orbital-decomposed (right) analysis of the electronic density of states in $Sn_2SbS_2I_3$. Negative COHP values (blue) indicate energy-lowering, bonding-type interactions, while positive values (orange) indicate anti-bonding character.

(JDOS) and optical transition dipole moment (TDM) at energies 0.3–0.5 eV above the direct band gap thus gives rise to a sharp increase in absorption coefficient at $E \geq 1.4$ eV (Fig. 5b and Fig. S16, ESI†).

This behaviour, we propose, is a likely cause of the apparent mismatch between the calculated fundamental band gap (E_g = 1.08 eV) and that measured by optical spectroscopy ($E_{Opt,Exp}$ = 1.41 eV). While the slow onset of absorption renders the unambiguous determination of an optical gap difficult, Tauc-plot fitting of the calculated absorption within the 1–1.8 eV range gives a best linear fit (with R^2 = 0.93) for an optical gap in the range 1.4–1.5 eV (Fig. S18, ESI†). Indeed, this plot closely resembles that measured by Nie *et al.*,[4] who also reported a large Urbach energy of 464 meV – which may in part be an artefact of the slow absorption onset.

To quantify the efficiency potential of this material as a photovoltaic (PV) absorber, based on the calculated electronic and optical properties, the maximum PV efficiency (η_{max}) as a function of film thickness was calculated using both the Spectroscopic Limited Maximum Efficiency (SLME)[60] and Blank *et al.*[61] metrics (Fig. 5c). As a consequence of the weak absorption onset, the attainable efficiency shows a strong dependence on film thickness, however this may be combatted through optimisation of the surface scattering properties. Using a Lambertian scattering surface, maximum efficiencies $\eta_{max} > 30\%$ are achieved at thicknesses $t > 0.5$ μm, demonstrating the potential application of this material class in high-performance earth-abundant solar cells. Importantly, this model assumes the radiative limit (*i.e.* internal quantum luminescence efficiency Q_i = 1), and so the presence of non-radiative recombination ($Q_i < 1$) will act to reduce the achievable efficiency and lead to a distinct optimal thickness in the range 0.5–5 μm (Fig. S19, ESI†).

Potential for defect tolerance

One of the primary origins of non-radiative electron–hole recombination is defects in the bulk crystal and at interfaces. By introducing electronic states within the bandgap, defects can facilitate carrier trapping and annihilation, thus reducing the open-circuit voltage (V_{oc}) and photovoltaic efficiency.[65–67] A primary driving factor behind the surge in research interest for ns^2-cation PIMs is their potential to exhibit defect tolerance – facilitating high efficiencies despite low-cost solution synthesis.[1,68,69] $Sn_2SbS_2I_3$ exhibits several material properties which are known to contribute to defect tolerance. Firstly, we find the cation s^2 and anion p orbitals interact to produce a valence band maximum of anti-bonding character. This bonding behaviour is illustrated by the Crystal Orbital Hamiltonian Population[70,71] (COHP) analysis shown in Fig. 6, which decomposes the electronic density of states into regions of bonding and anti-bonding orbital interactions. The cation ns^2-anion p anti-bonding interaction produces a high energy VBM, with an ionisation potential of 5.06 eV (Fig. S9, ESI†) – less than that of MAPI (5.70 eV),[72] SbSI (5.37 eV)[30] and Sb_2Se_3 (5.13 eV),[35] and slightly larger than that of $FaSnI_3$ (4.88 eV)[73] – favouring the formation of *shallow* acceptor defects which are innocuous to PV performance. The substantial mixed ionic-covalent character and lattice polarisability in $Sn_2SbS_2I_3$, discussed previously, results in a strong dielectric screening ($\varepsilon_{x,y,z}$ = [51.3, 18.2, 22.4]) that will limit the electrostatic interactions between defects and charge carriers, thus reducing the probability of carrier capture and trap-mediated recombination.[1,32]

One-dimensional atomic chain structures, exhibited by this (Fig. 1) and related materials such as Sb_2Se_3,[35] BiOI[32] and SbSI,[29,30] can yield benign grain boundaries, greatly reducing charge-carrier recombination in polycrystalline absorber materials.[32,74] The small electronic band gap ($E_g \sim 1.1$ eV), wide conduction and valence bands, and relatively small electron effective mass (m_e = 0.29) also favour defect-tolerant behaviour in this material.[1] Indeed, the presence of moderate defect tolerance is partially suggested by the impressive PV efficiency ($\eta > 4\%$) and photoluminescence lifetimes (>7 ns) obtained by Nie *et al.*[4] in the first experimental device fabrication for this material.

In conclusion, we present a theoretical characterisation of the $Sn_2SbS_2I_3$ photovoltaic absorber. While experimental investigations have reported a non-polar, *centrosymmetric Cmcm* crystal structure, we propose that this in fact represents a macroscopic average over multiple $Cmc2_1$ configurations. Crucially, this leads to the prediction of ferroelectricity, with promising implications for high-efficiency photovoltaic operation and other technological applications.

Through *ab initio* calculation of the electronic and optical properties, we identify an ideal electronic band gap for a photovoltaic absorber (E_g = 1.08 eV), with power-conversion efficiencies $\eta_{max} > 30\%$ at the radiative limit. These features, alongside several properties related to 'defect tolerance', present a promising outlook for the potential application of both this material and other unexplored members of the $A_2BCh_2X_3$ class. Considering only isoelectronic, earth-abundant and non-toxic substituents, there are in fact 36 possible elemental combinations for the quaternary group IV/V chalcohalide family (A = Sn, Ge; B = Sb, Bi; Ch = O, S, Se; X = I, Br, Cl) which may be synthesisable – the majority of which have not yet been

 This journal is © The Royal Society of Chemistry 2021

Open Access Article. Published on 05 July 2021. Downloaded on 6/18/2025 2:58:34 AM.
This article is licensed under a Creative Commons Attribution 3.0 Unported Licence.

investigated.‡ Thus the performance potential in this system opens a zoo of compositional permutations for solution-processed ferroelectric and optoelectronic devices.

Conflicts of interest

There are no conflicts to declare.

Acknowledgements

Seán R. Kavanagh thanks Dr Bonan Zhu for help with using the AiiDA infrastructure, Gabriel Krenzer for advice regarding molecular dynamics simulations, and Matthew Okenyi for useful discussions regarding Landau theory of hysteresis behaviour. SRK acknowledges the EPSRC Centre for Doctoral Training in the Advanced Characterisation of Materials (CDT-ACM)(EP/S023259/1) for funding a PhD studentship. CNS is grateful to the Ramsay Memorial Fellowship Trust and UCL Department of Chemistry for the funding of a Ramsay Fellowship. DOS acknowledges support from the EPSRC (EP/N01572X/1) and from the European Research Council, ERC (Grant No. 758345). AW acknowledges support from a National Research Foundation of Korea (NRF) grant funded by the Korean Government (MSIT) (2018R1C1B6008728). We acknowledge the use of the UCL Grace High Performance Computing Facility (Grace@UCL), the Imperial College Research Computing Service, and associated support services, in the completion of this work. *Via* membership of the UK's HEC Materials Chemistry Consortium, which is funded by the EPSRC (EP/L000202, EP/R029431, EP/T022213), this work used the ARCHER UK National Supercomputing Service (www.archer.ac.uk) and the UK Materials and Molecular Modelling (MMM) Hub (Thomas – EP/P020194 & Young – EP/T022213).

Notes and references

‡ The substitution of Sn with Pb, Sb with Bi and S with Se has been demonstrated for $Sn_2SbS_2I_3$.[10–12,75]

1 Y.-T. Huang, S. R. Kavanagh, D. O. Scanlon, A. Walsh and R. L. Z. Hoye, *Nanotechnology*, 2021, **32**, 132004.
2 M. Buchanan, *Nat. Phys.*, 2020, **16**, 996.
3 A. M. Ganose, C. N. Savory and D. O. Scanlon, *Chem. Commun.*, 2017, **53**, 20–44.
4 R. Nie, K. S. Lee, M. Hu, M. J. Paik and S. I. Seok, *Matter*, 2020, S2590238520304471.
5 R. Nie, R. R. Sumukam, S. H. Reddy, M. Banavoth and S. I. Seok, *Energy Environ. Sci.*, 2020, **13**, 2363–2385.
6 R. Nie, M. Hu, A. M. Risqi, Z. Li and S. I. Seok, *Adv. Sci.*, 2021, **8**, 2003172.
7 A. Zakutayev, J. D. Major, X. Hao, A. Walsh, J. Tang, T. K. Todorov, L. H. Wong and E. Saucedo, *J. Phys.: Energy*, 2021, **3**(3), 032003.
8 Y. C. Choi and K.-W. Jung, *Nanomaterials*, 2020, **10**, 2284.
9 J. Olivier-Fourcade, J. C. Jumas, M. Maurin and E. Philippot, *Z. Anorg. Allg. Chem.*, 1980, **468**, 91–98.
10 A. Ibanez, J.-C. Jumas, J. Olivier-Fourcade and E. Philippot, *J. Solid State Chem.*, 1984, **55**, 83–91.
11 V. Dolgikh, *Izv. Akad. Nauk SSSR, Neorg. Mater.*, 1985, **21**, 1211–1214.
12 V. I. Starosta, J. Kroutil and L. Beneš, *Cryst. Res. Technol.*, 1990, **25**, 1439–1442.
13 A. Kojima, K. Teshima, Y. Shirai and T. Miyasaka, *J. Am. Chem. Soc.*, 2009, **131**, 6050–6051.
14 G. Kresse and J. Hafner, *Phys. Rev. B: Condens. Matter Mater. Phys.*, 1993, **47**, 558–561.
15 G. Kresse and J. Hafner, *Phys. Rev. B: Condens. Matter Mater. Phys.*, 1994, **49**, 14251–14269.
16 G. Kresse and J. Furthmüller, *Comput. Mater. Sci.*, 1996, **6**, 15–50.
17 G. Kresse and J. Furthmüller, *Phys. Rev. B: Condens. Matter Mater. Phys.*, 1996, **54**, 11169–11186.
18 J. Klimeš, D. R. Bowler and A. Michaelides, *Phys. Rev. B: Condens. Matter Mater. Phys.*, 2011, **83**, 195131.
19 A. Lozano, B. Escribano, E. Akhmatskaya and J. Carrasco, *Phys. Chem. Chem. Phys.*, 2017, **19**, 10133–10139.
20 S. A. Tawfik, T. Gould, C. Stampfl and M. J. Ford, *Phys. Rev. Mater.*, 2018, **2**, 034005.
21 F. Tran, L. Kalantari, B. Traoré, X. Rocquefelte and P. Blaha, *Phys. Rev. Mater.*, 2019, **3**, 063602.
22 S. Jaśkaniec, S. R. Kavanagh, J. Coelho, S. Ryan, C. Hobbs, A. Walsh, D. O. Scanlon and V. Nicolosi, *npj 2D Mater. Appl.*, 2021, **5**, 1–9.
23 J. Heyd, G. E. Scuseria and M. Ernzerhof, *J. Chem. Phys.*, 2003, **118**, 8207–8215.
24 J. Harl, L. Schimka and G. Kresse, *Phys. Rev. B: Condens. Matter Mater. Phys.*, 2010, **81**, 115126.
25 M. Kaltak, J. Klimeš and G. Kresse, *J. Chem. Theory Comput.*, 2014, **10**, 2498–2507.
26 P. Borlido, J. Schmidt, A. W. Huran, F. Tran, M. A. L. Marques and S. Botti, *npj Comput. Mater.*, 2020, **6**, 1–17.
27 A. V. Krukau, O. A. Vydrov, A. F. Izmaylov and G. E. Scuseria, *J. Chem. Phys.*, 2006, **125**, 224106.
28 A. Jain, S. P. Ong, G. Hautier, W. Chen, W. D. Richards, S. Dacek, S. Cholia, D. Gunter, D. Skinner, G. Ceder and K. a. Persson, *APL Mater.*, 2013, **1**, 011002.
29 K. T. Butler, J. M. Frost and A. Walsh, *Energy Environ. Sci.*, 2015, **8**, 838–848.
30 K. T. Butler, S. McKechnie, P. Azarhoosh, M. van Schilfgaarde, D. O. Scanlon and A. Walsh, *Appl. Phys. Lett.*, 2016, **108**, 112103.
31 A. M. Ganose, K. T. Butler, A. Walsh and D. O. Scanlon, *J. Mater. Chem. A*, 2016, **4**, 2060–2068.
32 H. Shi, W. Ming and M.-H. Du, *Phys. Rev. B*, 2016, **93**, 104108.
33 A. Walsh, D. J. Payne, R. G. Egdell and G. W. Watson, *Chem. Soc. Rev.*, 2011, **40**, 4455–4463.
34 C. N. Savory and D. O. Scanlon, *J. Mater. Chem. A*, 2019, **7**, 10739–10744.
35 C. H. Don, H. Shiel, T. D. C. Hobson, C. N. Savory, J. E. N. Swallow, M. J. Smiles, L. A. H. Jones, T. J. Featherstone, P. K. Thakur, T.-L. Lee, K. Durose, J. D. Major, V. R. Dhanak, D. O. Scanlon and T. D. Veal, *J. Mater. Chem. C*, 2020, **8**, 12615–12622.
36 G. Rhodes, *Crystallography Made Crystal Clear: A Guide for Users of Macromolecular Models*, Elsevier, Amsterdam, 3rd edn, 2006.

Open Access Article. Published on 05 July 2021. Downloaded on 6/18/2025 2:58:34 AM.
This article is licensed under a Creative Commons Attribution 3.0 Unported Licence.

37 K. B. Spooner, M. Einhorn and D. W. Davies, GitHub:SMT-G_UCL/ThermoPlotter, 2020.
38 R. L. Z. Hoye, P. Schulz, L. T. Schelhas, A. M. Holder, K. H. Stone, J. D. Perkins, D. Vigil-Fowler, S. Siol, D. O. Scanlon, A. Zakutayev, A. Walsh, I. C. Smith, B. C. Melot, R. C. Kurchin, Y. Wang, J. Shi, F. C. Marques, J. J. Berry, W. Tumas, S. Lany, V. Stevanović, M. F. Toney and T. Buonassisi, *Chem. Mater.*, 2017, **29**, 1964–1988.
39 J. Harl and G. Kresse, *Phys. Rev. Lett.*, 2009, **103**, 056401.
40 H. T. Stokes, D. M. Hatch and B. J. Campbell, *ISODISTORT*, ISOTROPY Software Suite.
41 B. J. Campbell, H. T. Stokes, D. E. Tanner and D. M. Hatch, *J. Appl. Crystallogr.*, 2006, **39**, 607–614.
42 R. D. King-Smith and D. Vanderbilt, *Phys. Rev. B: Condens. Matter Mater. Phys.*, 1993, **47**, 1651–1654.
43 H. H. Wieder, *Phys. Rev.*, 1955, **99**, 1161–1165.
44 A. Stroppa, C. Quarti, F. De Angelis and S. Picozzi, *J. Phys. Chem. Lett.*, 2015, **6**, 2223–2231.
45 A. A. Grekov, A. I. Rodin and V. M. Fridkin, *Appl. Phys. Lett.*, 1969, **14**, 119–120.
46 J. M. Frost, K. T. Butler, F. Brivio, C. H. Hendon, M. van Schilfgaarde and A. Walsh, *Nano Lett.*, 2014, **14**, 2584–2590.
47 N. A. Spaldin, *J. Solid State Chem.*, 2012, **195**, 2–10.
48 D. H. Fabini, G. Laurita, J. S. Bechtel, C. C. Stoumpos, H. A. Evans, A. G. Kontos, Y. S. Raptis, P. Falaras, A. Van der Ven, M. G. Kanatzidis and R. Seshadri, *J. Am. Chem. Soc.*, 2016, **138**, 11820–11832.
49 J. Brgoch, A. J. Lehner, M. Chabinyc and R. Seshadri, *J. Phys. Chem. C*, 2014, **118**, 27721–27727.
50 H. Jónsson, G. Mills and K. W. Jacobsen, *Classical and Quantum Dynamics in Condensed Phase Simulations*, World Scientific, 1998, pp. 385–404.
51 S. Song, H. M. Jang, N.-S. Lee, J. Y. Son, R. Gupta, A. Garg, J. Ratanapreechachai and J. F. Scott, *NPG Asia Mater.*, 2016, **8**, e242.
52 B. Chen, J. Shi, X. Zheng, Y. Zhou, K. Zhu and S. Priya, *J. Mater. Chem. A*, 2015, **3**, 7699–7705.
53 I. Grinberg, D. V. West, M. Torres, G. Gou, D. M. Stein, L. Wu, G. Chen, E. M. Gallo, A. R. Akbashev, P. K. Davies, J. E. Spanier and A. M. Rappe, *Nature*, 2013, **503**, 509–512.
54 P. S. Brody, *Ferroelectrics*, 1975.
55 T. S. Sherkar and L. J. A. Koster, *Phys. Chem. Chem. Phys.*, 2016, **18**, 331–338.
56 F. Zheng, H. Takenaka, F. Wang, N. Z. Koocher and A. M. Rappe, *J. Phys. Chem. Lett.*, 2015, **6**, 31–37.
57 S. Picozzi, *Front. Phys.*, 2014, **2**, 10.
58 C. W. Myung, J. Yun, G. Lee and K. S. Kim, *Adv. Energy Mater.*, 2018, **8**, 1702898.
59 A. M. Ganose, A. J. Jackson and D. O. Scanlon, *J. Open Source Software*, 2018, **3**, 717.
60 L. Yu and A. Zunger, *Phys. Rev. Lett.*, 2012, **108**, 068701.
61 B. Blank, T. Kirchartz, S. Lany and U. Rau, *Phys. Rev. Appl.*, 2017, **8**, 024032.
62 W. Shockley and H. J. Queisser, *J. Appl. Phys.*, 1961, **32**, 510–519.
63 D. R. Lide, *CRC Handbook of Chemistry and Physics*, CRC Press, Florida, 84th edn, 2003.
64 Z. Li, S. R. Kavanagh, M. Napari, R. G. Palgrave, M. Abdi-Jalebi, Z. Andaji-Garmaroudi, D. W. Davies, M. Laitinen, J. Julin, M. A. Isaacs, R. H. Friend, D. O. Scanlon, A. Walsh and R. L. Z. Hoye, *J. Mater. Chem. A*, 2020, **8**, 21780–21788.
65 S. R. Kavanagh, A. Walsh and D. O. Scanlon, *ACS Energy Lett.*, 2021, **6**, 1392–1398.
66 S. Kim, J. A. Márquez, T. Unold and A. Walsh, *Energy Environ. Sci.*, 2020, 1481–1491.
67 C. Freysoldt, B. Grabowski, T. Hickel, J. Neugebauer, G. Kresse, A. Janotti and C. G. Van de Walle, *Rev. Mod. Phys.*, 2014, **86**, 253–305.
68 A. Walsh and A. Zunger, *Nat. Mater.*, 2017, **16**, 964–967.
69 R. C. Kurchin, P. Gorai, T. Buonassisi and V. Stevanović, *Chem. Mater.*, 2018, **30**, 5583–5592.
70 V. L. Deringer and R. Dronskowski, in *Comprehensive Inorganic Chemistry II (Second Edition)*, ed. J. Reedijk and K. Poeppelmeier, Elsevier, Amsterdam, 2013, pp. 59–87.
71 R. Dronskowski and P. E. Bloechl, *J. Phys. Chem.*, 1993, **97**, 8617–8624.
72 K. T. Butler, J. M. Frost and A. Walsh, *Mater. Horizons*, 2015, **2**, 228–231.
73 Z. Zhao, F. Gu, Y. Li, W. Sun, S. Ye, H. Rao, Z. Liu, Z. Bian and C. Huang, *Adv. Sci.*, 2017, **4**, 1700204.
74 Y. Zhou, L. Wang, S. Chen, S. Qin, X. Liu, J. Chen, D.-J. Xue, M. Luo, Y. Cao, Y. Cheng, E. H. Sargent and J. Tang, *Nat. Photonics*, 2015, **9**, 409–415.
75 S. M. Islam, C. D. Malliakas, D. Sarma, D. C. Maloney, C. C. Stoumpos, O. Y. Kontsevoi, A. J. Freeman and M. G. Kanatzidis, *Chem. Mater.*, 2016, **28**, 7332–7343.

This journal is © The Royal Society of Chemistry 2021